Anisotropic stress history effects in erodible sediment beds

Sophie Bodek[1], Dong Wang[2], Mark D. Shattuck[3], Corey S. O'Hern[2,4,5], Nicholas T. Ouellette[1]

[1]Department of Civil and Environmental Engineering, Stanford University, Stanford, CA 94305
[2]Department of Mechanical Engineering, Yale University, New Haven, CT 06520
[3]Benjamin Levich Institute and Physics Department, The City College of New York, New York, NY 10031
[4]Department of Applied Physics, Yale University, New Haven, CT 06520
[5]Department of Physics, Yale University, New Haven, CT 06520

Key Points:

- We use particle tracks from laboratory experiments to study grain velocities and activity subject to fluid flows from different directions
- Our sand bed strengthens under unidirectional flows, but exhibits weakening as the offset between "conditioning" and eroding flows increases
- The stress history imparted by directional flows impacts both the number of active grains and bedload velocity

Corresponding author: Sophie Bodek, sbodek@stanford.edu

Abstract

Bedload transport occurs when the shear stress, or non-dimensional Shields stress, imparted by a fluid onto a sediment bed exceeds a critical value for sediment entrainment. The history of fluid stress imparted onto a sediment bed influences this critical Shields stress, with bed strengthening occurring under unidirectional flows and bed weakening occurring when the flow direction is reversed. In this study, we examine directional strengthening and weakening in a sediment bed for multiple fluid stress orientations using a rotating bed of sand in a laboratory flume. This sediment bed is exposed to an initial subcritical conditioning flow followed by a subsequent erosive flow at an offset angle. We identify the particle trajectories of a population of sediment grains to measure their velocity, activity, and associated bulk statistics. We confirm bed strengthening (i.e., lower grain velocity and activity) in the unidirectional case, especially for flows at or below the nominal critical Shields stress. As the angular offset increases between the conditioning and erosive flows, both grain velocity and activity increase, with the greatest bed weakening at offsets of 135° and 180°. Our results confirm that stress history is stored anisotropically in the sediment bed, supporting mechanisms such as shear jamming where an anisotropic granular fabric develops in response to shear. Our results have implications for predicting sediment transport in natural settings where flows can come from many directions, and for improving our understanding of how subcritical and critical fluid-imposed stresses can modify the grain contact and force networks in geophysical contexts.

Plain Language Summary

Bedload transport, or the movement of sediment near the surface of a sand or gravel bed, occurs when shearing forces delivered by a flowing fluid overcome the forces keeping the sediment in place. The critical shear stress depends on many variables, including the history of fluid flow over the bed. Sustained slow flows can strengthen a sediment bed, resulting in reduced bedload transport and a higher critical shear stress, even when the bed appears mostly static. Recent studies have also shown that a slow flow in one direction followed by a rapid flow in the opposite direction results in bed weakening and greater bedload transport. To explore the influence of flow history and direction on the critical shear stress, we use a laboratory flume with a rotating sediment bed. This sediment bed is subjected to a slow flow, then rotated to a set angle and exposed to an erosive flow. We identify the tracks of individual sediment grains to analyze grain velocity and activity. Thus, we can quantify the differences in sediment bed behavior due to the stress history imparted by previous flow directions. This knowledge can improve sediment transport predictions in systems with multiple flow directions, like coastal environments.

1 Introduction

The transport of sediment by flowing water is a fundamental physical process that shapes many of Earth's landscapes and has broad implications in environmental, ecological, and engineering contexts. The accurate prediction and evaluation of sediment transport thresholds and rates, however, remains an ongoing challenge due to the complex interactions between the granular bed material and turbulent, open-channel flow (see Pähtz et al., 2020). The typical framework for predicting the onset of sediment motion relies on an estimate of the Shields stress τ_*, the ratio of the fluid-imposed bed stress to the buoyancy-reduced gravitational stress (Shields, 1936). When the Shields stress reaches a critical value, τ_{*cr} (a threshold that is also dependent on the particle Reynolds number), sediment grains begin to be mobilized into bedload transport as the forces imposed by the driving fluid overcome those resisting entrainment (e.g., Wiberg & Smith, 1987; Dey, 1999). Although choosing a single value for this threshold of motion has significant utility and is widely assumed in bedload transport models (e.g., Ashida & Michiue,

1973; Engelund & Fredsøe, 1976; Luque & Van Beek, 1976; Meyer-Peter & Müller, 1948; Wong & Parker, 2006), challenges arise due to the considerable variation in reported shear stresses at the onset of sediment transport in both field and flume studies (Buffington & Montgomery, 1997) and the diminished predictive power of these models near the threshold of grain motion (Recking et al., 2012). Thus, this framework, while useful, is ultimately insufficient in many contexts (e.g., Lavelle & Mofjeld, 1987; Yager et al., 2018). Further, since much of sediment transport in gravel-bed rivers is thought to occur at near-threshold conditions (Parker, 1979; Phillips & Jerolmack, 2016), an accurate assessment of τ_{*cr} can improve sediment transport predictions in fluvial environments.

The variable nature of the bed surface (e.g., Kirchner et al., 1990) and turbulent fluctuations in the flow (e.g., Einstein & El-Samni, 1949) give rise to complex physical mechanisms governing sediment entrainment and transport that can be highly variable across spatial and temporal scales (Sumer et al., 2003; Diplas et al., 2008; Papanicolaou et al., 2001; Escauriaza et al., 2023; Cameron et al., 2020). This temporal variability has been observed in both experimental and natural systems, where τ_{*cr} varies with the history of fluid stress (e.g., Turowski et al., 2011; Mao, 2018). Hysteresis can occur in sediment transport rates during individual floods (Roth et al., 2014; Pretzlav et al., 2020; Mao et al., 2014) and cause variations in the onset of sediment motion due to seasonal variability in flood magnitudes and intermittency (Reid et al., 1985; Masteller et al., 2019). Alternate representations of the critical Shields stress may assist in understanding these time-dependent dynamics. Clark et al. (2017) interpreted τ_{*cr} as the stress at which mobile grains can no longer find a static configuration—an approach that incorporates inertial effects from particle-bed interactions. Houssais et al. (2015), meanwhile, interpreted τ_{*cr} as the transition from creep to a dense granular flow, thus showing the presence of slow and sporadic grain movements within both the bed surface and subsurface.

While the traditional framework for estimating the onset of sediment transport assumes that granular beds do not undergo significant reorganization when the bed stress is below the threshold for bulk motion (Gomez, 1983), field observations have revealed that sediment flux during floods is (at least partially) dependent on the duration of inter-event slow flows (Reid et al., 1985). In natural gravel-bed rivers, both Oldmeadow and Church (2006) and Masteller et al. (2019) describe a cycle where bed stability increases and bedload transport decreases during drier times of year when streamflow is slow and bankfull floods are uncommon. Subsequently, during spring snowmelt or rainy periods when bankfull or greater floods tend to occur, these rapid flows disrupt any structure or orientation that may have developed and "reset" the bed to a more mobile and unstructured state. Laboratory experiments have since confirmed that τ_{*cr} is sensitive to the magnitude and duration of prior flows, with beds typically exhibiting a strengthening behavior when the fluid flow always comes from the same direction, even in the absence of measurable sediment transport (Haynes & Pender, 2007; A. Ockelford et al., 2019; Paphitis & Collins, 2005; Monteith & Pender, 2005; A.-M. Ockelford & Haynes, 2013; Masteller & Finnegan, 2017). The term *stress history* (also occasionally called *memory stress*) generally describes the effects of these sub-threshold flows applied to a sediment bed, and incorporates both the duration and magnitude of shear stress applied to the bed (Monteith & Pender, 2005).

In geophysical contexts, the mechanism for strengthening during subcritical flows has generally been attributed to subtle reorganization of the sediment bed, leading both to a coarser surface and more stable grain configurations (e.g., Masteller & Finnegan, 2017; Haynes & Pender, 2007; A.-M. Ockelford & Haynes, 2013). A well-known example is the formation of a surficial "armor", a phenomenon that is most apparent in graded rivers where granular segregation results in a coarse surface layer overlying a finer subsurface (e.g., Parker & Klingeman, 1982; Ferdowsi et al., 2017). We can also consider stress history as a type of strain hardening, as beds experience compaction when driven as bedload by above-critical flows (Charru et al., 2004) and as creep by subcritical flows

(Allen & Kudrolli, 2018). Additionally, as the bed experiences a directional boundary shear, grain contacts can be preferentially loaded forming anisotropic force chains that bear internal stresses and stabilize the material in the direction of shear (Bi et al., 2011; Cates et al., 1998; Majmudar & Behringer, 2005; Behringer & Chakraborty, 2018). Continued loading can produce a fragile, then shear jammed state—conditions where the stability of the granular material can be disrupted if the direction of loading changes (Bi et al., 2011). In systems with cyclic shear, the grain network must rearrange upon change of direction of the applied shear, which further motivates weakening (Slotterback et al., 2012). Recent experiments examining the evolution of τ_{*cr} in granular beds subject to forward and reverse fluid shear directions have observed bed weakening (i.e., lower τ_{*cr} or increased bedload transport) when the flow direction is reversed (Galanis et al., 2022; Cúñez et al., 2022). Cúñez et al. (2022), who also examined stress history effects from an oscillating flow, found that the granular fabric developed during the oscillating flow was weaker than the anisotropic fabric developed under unidirectional flow, despite greater compaction of the bed material.

In this article, we investigate the effect of directional stress history on thresholds for incipient grain motion in sediment beds. We carry out experiments in a laboratory flume where the sediment bed is subject to a subcritical conditioning flow, followed by an erosive flow from an offset direction. In comparison to prior studies that examine the evolution of bed stability subject to unidirectional and reversed flows, our experimental setup allows for mobilizing flow directions that are offset by any angle from the initial subcritical flow direction. Further, we investigate the anisotropic mechanisms for storing stress history in a geophysical context by using natural sand grains and a turbulent shearing flow. By examining grain motions during the transition from below threshold to incipient motion to bedload transport, we are able to quantify grain activity. Further, we use collective grain velocity statistics to compare the number of mobilized grains and characteristic grain velocity for the various conditioning directions. While perhaps less applicable to the standard single-thread alluvial river, the setup of this study applies to tidally-influenced channels, braided rivers, and even floodwaters that enter abandoned channels or floodplains from unusual directions. Our results imply that sediment transport may be enhanced in these environments compared to predictions from a standard Shields framework.

2 Methods

2.1 Experimental Configuration and Protocol

Experiments were conducted in a recirculating, open channel flume. The inflow is controlled by a variable speed pump that fills a constant-head tank, which drives the water through a diffuser, homogenizing grids, and a two-dimensional constriction into a rectangular channel section. The glass-walled test section has a length of 3 m and width of 0.6 m, with additional 1.5 m long buffer sections to mitigate entrance and exit effects. The flow rate and depth are set by both the pump and the height of a sharp-crested downstream control weir. At rest, the flow depth was 17.5 cm. A full description of this facility was initially documented in O'Riordan et al. (1993) and an illustrative schematic is shown in Figure 1a.

The test section of the flume has a false bottom, allowing for the installation of an inset sediment bed, the edge of which was mounted flush with the surrounding floor (Figure 1b). The leading edge was 1.3 m from the start of the test section, and the inset bed was centered within the channel cross section. The sediment bed consisted of a circular dish that was 45.7 cm (18 in) in diameter and 7.6 cm (3 in) deep; the dish was filled with medium to coarse-sized sand, a population of which was painted fluorescent orange for imaging purposes (Figure 1c). The granular bed and particle imaging and tracking methodologies are discussed further in Section 2.3. The sediment bed was mounted on

a rotating turntable base, permitting multiple orientations of the sand bed relative to the flume.

A camera was mounted above the center of the sediment bed to record the motions of the sand grains. Any secondary flows produced by the transition between the smooth acrylic floor and the start of the sediment bed decayed before reaching the camera field of view (FOV), located 16 cm from the leading edge of the bed. To ensure that the camera had a clear view of the sand below, a small glass window (referred to as the "boat") was placed on the free surface of the flow above the sediment bed. This placement minimized image distortions due to light refraction off ripples in the free surface. An acoustic Doppler velocimeter (ADV) was mounted behind the boat over the downstream portion of the sediment bed to collect flow velocity measurements during experiments. The test section configuration is shown in Figure 1b and 1c.

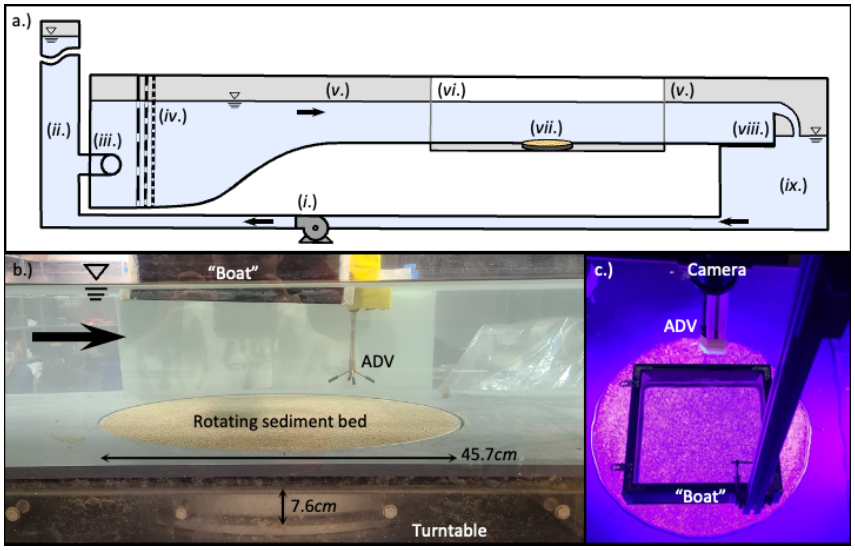

Figure 1. Recirculating flume facility with installed sediment bed. (a) Schematic depicting the entire flume facility, including: (*i*) variable-speed pump, (*ii*) constant-head tank, (*iii*) diffuser and inlet, (*iv*) homogenizing grids, (*v*) 1.5 m long buffer sections, (*vi*) 3 m long glass-walled test section, (*vii*) inset rotating sediment bed, (*viii*) sharp-crested control weir, and (*ix*) reservoir. (b) Close-up of the portion of the test section with the inset sediment bed and nearby instrumentation. (c) Top-down view of the sediment bed illuminated by ultraviolet lights, showing the fluorescent-painted grains.

We were careful to prepare the sediment bed in the same way for each experimental run. Prior to each experiment, a stirrer was used to agitate the submerged sand bed and break up any structures that may have been present within the granular material. We then leveled the sediment bed by dragging a stiff piece of mesh over the bed surface. For all but one experimental case, we subject the bed to a subcritical "conditioning flow" for 20 min. This conditioning flow had a Shields number that was approximately 75−80% of the nominal critical value for our sediment bed; this critical value, $\tau_{*cr} \approx 0.033$, was estimated using a Shields curve analysis. Although several grains were observed to jiggle or even roll one or two grain diameters during the course of the conditioning, significant grain motion was not observed at this flow velocity.

Following this 20 min period, we stopped the flow and manually rotated the sand bed by 0°, 45°, 90°, 135°, or 180° relative to the initial conditioning flow direction. The

rotating sediment bed apparatus was stationary during both the conditioning phase and the subsequent "erosive flow". The rotation thus only changed the direction of the erosive flow relative to the initial conditioning flow. To produce the erosive flow, the speed of the pump was raised in steps, such that the flow velocity increased in increments of approximately $\sim 1.4{-}2.2$ cm/s, measured at 2 cm above the sediment bed. After each step up, the flow was allowed to stabilize for 1 min; then, a 45 sec video of the sediment motions was collected. A total of 9 flow velocity intervals were used when inducing sediment transport, starting at the conditioning flow velocity ($\tau_* = 0.026$) and increasing to an above-threshold state where bedload was readily observed ($\tau_* = 0.05$). The sediment transport regime in the flume was limited to bedload, i.e. the grains were not observed to travel in suspension. The bed was always reset before any new experiment was conducted; thus, observations of sediment motion were made on a newly prepared and conditioned bed, regardless of turntable orientation. A total of 8 trials were conducted for the 6 experimental cases—control (no conditioning), 0°, 45°, 90°, 135°, and 180° relative to the initial conditioning flow direction.

2.2 Flow Characterization

We characterized the streamwise flow velocity using a Nortek Vectrino Profiler, a type of acoustic Doppler profiling velocimeter (ADV). This ADV profiling instrument was mounted over the sediment bed as shown in Figure 1b. The flow conditions at 10 settings of the variable speed pump were measured in a series of calibration runs (3 runs per pump setting). During these calibration runs, the flume was heavily seeded with neutrally buoyant glass microspheres to better reflect acoustic waves emitted by the instrument. The ADV profiler measured a 3 cm velocity profile above the sediment bed, with a 1 mm vertical resolution; measurements were collected at a rate of 65 Hz and time-averaged over a 10 min period (Figure 2a).

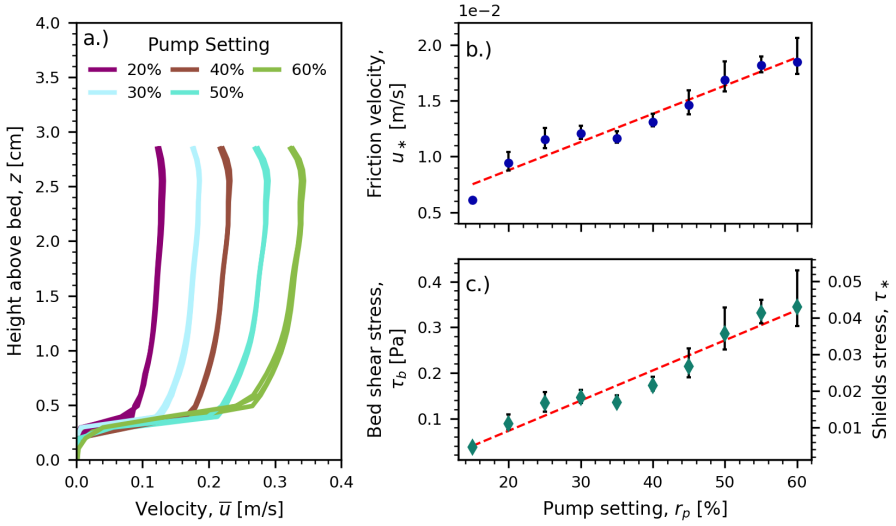

Figure 2. (a) Measured time-averaged velocity profiles for 5 pump settings used to calibrate flow parameters; the pump setting value indicates the percentage of the maximum pump output. (b) The friction velocity u_* computed for each pump setting using the Law of the Wall. The red dashed line indicates a linear best fit given by $u_* = 2.5\times10^{-4} r_p + 3.7\times10^{-3}$. (c) Bed shear stress τ_b and Shields stress τ_* as a function of pump setting. The red dashed line indicates a linear best fit given by $\tau_b = 6.6\times10^{-3} r_p - 5.9\times10^{-2}$. Error bars indicate the range of values calculated.

We determined the friction velocity, u_*, by fitting the Law of the Wall to our time-averaged velocity profiles, namely

$$u = \frac{u_*}{\kappa} \ln\left(\frac{z}{z_o}\right) \tag{1}$$

where u is the flow velocity, z is the height above the sediment bed, z_o is the roughness length (also fit to measured velocity profiles), and $\kappa = 0.41$ is the von Karman constant. It was found that the friction velocity increased approximately linearly with pump setting (Figure 2b). From the friction velocity, we can calculate the bed stress, τ_b, and Shields number, τ_*, as given by

$$u_* = \sqrt{\frac{\tau_b}{\rho}} \tag{2}$$

and

$$\tau_* = \frac{\tau_b}{(\rho_s - \rho) g D_{50}} \tag{3}$$

where ρ is the fluid density, ρ_s is the sediment density, g is acceleration due to gravity, and D_{50} is the median grain size of the sediment bed. Since velocity profiles were not directly measured for all flow velocity intervals used in the previously described experimental procedure, we used a linear fit between the percentage of the maximum pump output and the friction velocity (Figure 2b), as well as pump output and bed shear stress (Figure 2c) to define u_*, τ_b and τ_*.

During experiments, a Nortek Vectrino ADV was mounted above the sediment bed in the same location as the ADV profiler (Figure 1b). The Vectrino instrument collected velocity measurements at a single point with a sample rate of 200 Hz that was subsampled to 60 Hz. Data collected during each experiment were compared against the flow velocity for each interval calculated using the calibration described above; good agreement was observed.

The particle Reynolds number $Re_p = u_* D_{50}/\nu$ ranged from $6.8 - 10.6$ for our experimental conditions, where the kinematic viscosity of water is approximately $\nu = 10^{-6}$ m^2/s. Thus, our experiments were conducted in a hydraulically transitional flow.

2.3 Sediment Bed and Particle Tracking

The sediment bed consisted of commercially available quartz sand ($\rho_s = 2650$ kg/m^3) with a median grain size of $D_{50} = 0.495$ mm and uniform distribution $\sigma_g = (D_{84}/D_{16})^{0.5} = 1.24$ as measured using a Camsizer X2 instrument (García, 2013). To detect individual sand grains, a population of the sand was spray painted a fluorescent orange color. The orange-painted grains were mixed with unpainted sand in a 17/83 mixture by volume.

The bed was imaged using a FLIR Flea3 monchrome camera (model FL3-U3-13Y3M-C) with an SMC Pentax-M 28 mm f2.8 lens that was mounted above the center of the sediment bed looking vertically down through the boat (Figure 1c). During experiments, the sediment bed was illuminated by an ultraviolet light in a dark room, such that the painted sand grains glowed orange (Kelley et al., 2023). The camera lens was fitted with an optical band pass filter to collect light emitted by the fluorescent paint; thus, these grains appeared bright on the dark background of unpainted sand. Images measuring 1280×1048 pixels with a spatial resolution of 0.085 mm per pixel were captured at 120 fps.

We reconstructed the particle trajectories of the fluorescing grains using a multi-frame predictive particle-tracking algorithm (Ouellette et al., 2006); grain velocities were then computed from these trajectories via convolution with a smoothing and differentiating kernel (Mordant et al., 2004). Particle tracking has been used to characterize grain behavior in other sediment transport studies (e.g., Salevan et al., 2017; Lajeunesse et al., 2010; Shim & Duan, 2017; Radice et al., 2017), including those investigating stress history effects (Galanis et al., 2022). Parameters specified for the tracking algorithm of Ouellette

et al. (2006) included a threshold intensity such that approximately 800 grains were identified in each frame, as well as a minimum and maximum particle area corresponding to the sieve sizes used to constrain the grain size distribution (0.3 mm and 0.8 mm). While this algorithm kinematically predicts particle trajectories over multiple frames, we specify a search radius in the predicted particle position if the tracked grain is not immediately found. This search radius was conservatively set for each pump setting and manual visual inspection of a subset of images with grain trajectories was used to confirm track accuracy (Figure 3). We note that the conservative selection of search radius results in broken trajectories over longer hops, but avoids drawing false tracks between nearby stationary particles. In the analysis described below, we focus on bulk statistics of the grain velocity and activity and do not consider metrics from individual tracks; thus, these broken linkages are not a significant issue for our analyses.

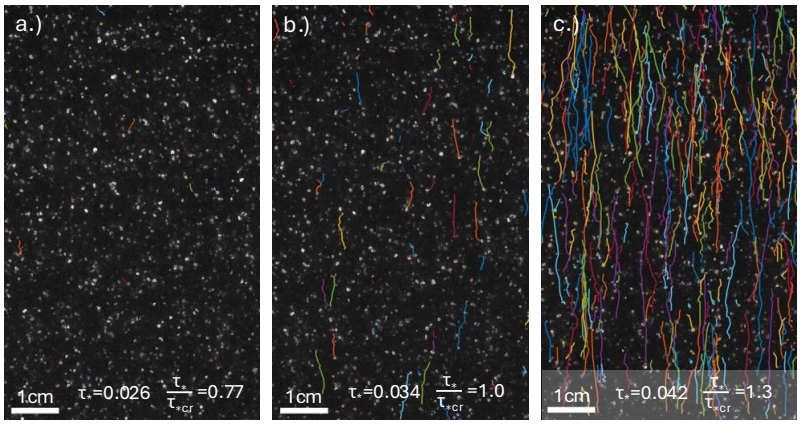

Figure 3. Example sediment tracks from the particle-tracking analysis overlaid onto images of the underlying sediment bed for three flow velocity intervals: (a) the conditioning flow velocity where $\tau_* = 0.026$, (b) the critical flow velocity where $\tau_* = 0.034$, and (c) an above-critical flow velocity where $\tau_* = 0.042$. All tracks longer than 10 frames in a 45 sec movie are shown with individual tracks depicted in various colors. The raw images show fluorescing sand grains in the center of the field of view; the physical dimensions are 8.75 cm in the streamwise direction (vertical) and 5.5 cm in the spanwise direction (horizontal). The flow direction is from the bottom to the top of the images.

3 Results

3.1 Conditioning Flows

During the 20 min conditioning flow, videos of the sediment bed were collected at 5 min intervals. Using this series of videos, we can investigate the grain dynamics during the subcritical conditioning period. We quantify grain motion using the mean grain velocity $\langle \bar{u}_g \rangle$, which is calculated by averaging the instantaneous streamwise velocity of each grain identified by the particle-tracking algorithm over each frame of the 45 sec video. This metric captures the motions of both grains actively transported through rolls and hops, as well as those that are largely stationary or only jiggling in place. Thus, $\langle \bar{u}_g \rangle$ tends to be much smaller than the typical velocity of a moving grain, as the sediment bed is largely immobile at subcritical conditions. The measured values of $\langle \bar{u}_g \rangle$ over the conditioning period are shown in Figure 4a.

In addition to the grain velocity, we can also characterize grain motion by counting the number of active grains in a given frame per unit area, averaged over all frames in the 45 sec video. Termed "grain activity", $\langle \bar{n}_g \rangle$, this metric is similar to the surface density of moving particles introduced by Lajeunesse et al. (2010) or the particle number activity used by Roseberry et al. (2012). A grain is considered active if its instantaneous velocity is above a threshold velocity that varies depending on bulk sediment velocity statistics. The selection of this threshold velocity is discussed further in Section 3.4 below. We can also sum the number of active grains in each frame to determine the total number of active grains over the course of a 45 sec video (Figure 4b).

Over the course of the 20 min conditioning period, we can see that both the average grain velocity and grain activity decrease, with a significant reduction in both measurements occurring in the first 5 minutes. The average grain velocity experiences a nearly 60% reduction in this initial quarter, then begins to plateau over the next 10 minutes before decreasing again in the final quarter of the conditioning period. The number of active grains follows a similar pattern, with an initial reduction of 63% in the first 5 minutes, followed by a more gradual decline in grain activity over the subsequent 15 minutes. The total number of active grains decreases by an order of magnitude over the entire conditioning period, with 228 active grains in the first 45 sec and only 27 active grains in the final 45 sec of the conditioning period.

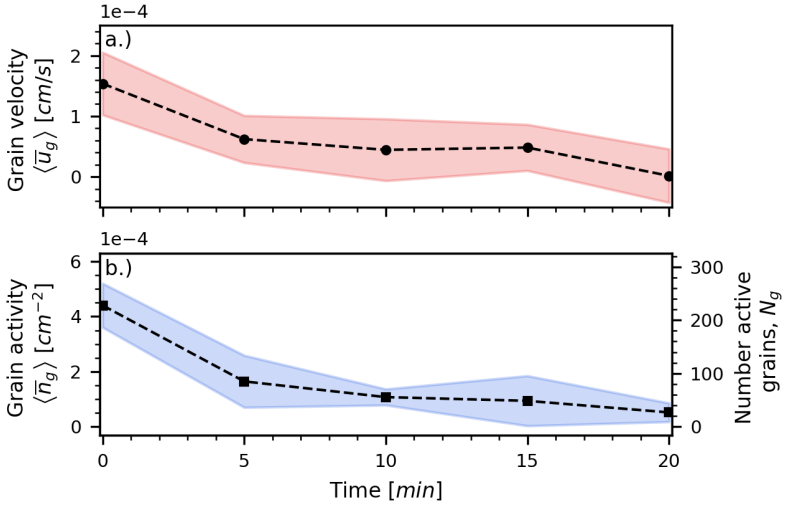

Figure 4. Sediment bed activity over the subcritical conditioning period: (a) mean grain velocity $\langle \bar{u}_g \rangle$ averaged over all identified grains in each video; (b) grain activity $\langle \bar{n}_g \rangle$ (left ordinate axis) and total number of active grains N_g (right ordinate axis) in each video. Shaded regions indicate 95% confidence intervals for both plots; four trials were completed.

3.2 Grain Velocities

Using the same measurement of mean grain velocity $\langle \bar{u}_g \rangle$ as described in the previous section, we can characterize the behavior of the sediment bed during the steps-up in speed of the erosive flow. The data in Figure 5 show the mean grain velocity for each orientation of the sediment bed relative to the flume test section, with each panel showing mean grain velocity measured at one of the nine incremental flow speeds. For all orientations (control, 0°, 45°, 90°, 135°, and 180°), the mean grain velocity becomes faster as the flow speed, and thus the bed stress and Shields stress, increases. For the unconditioned control case, the approximate value of the critical Shields number is consistent

with a traditional Shields curve analysis, where $\tau_{*cr} = 0.033$ (Buffington & Montgomery, 1997).

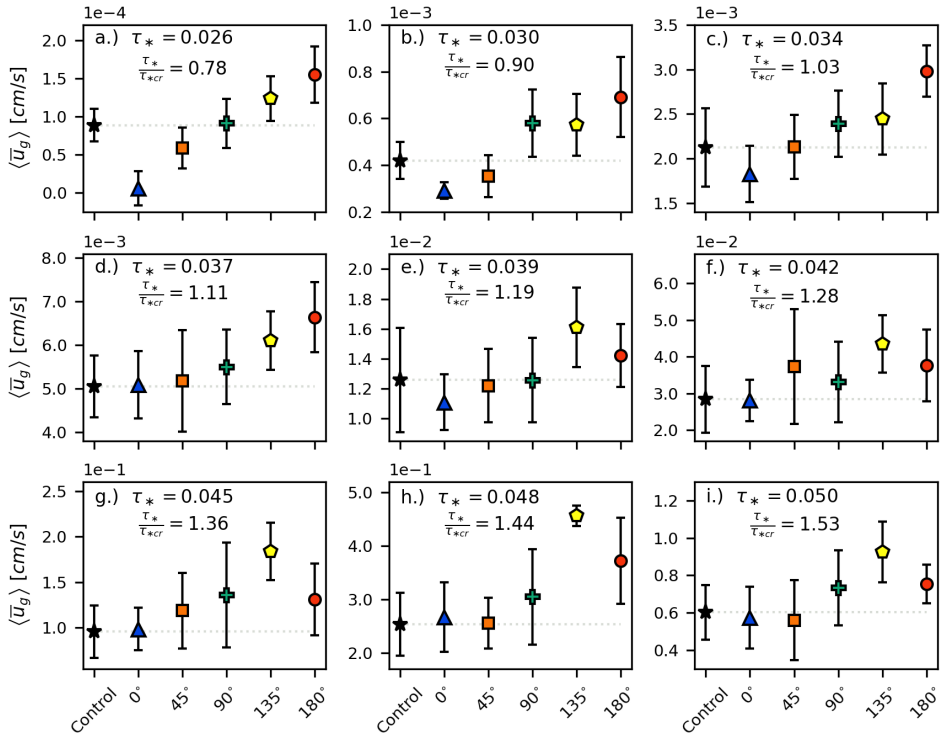

Figure 5. Mean grain velocity averaged over all identified grains $\langle \bar{u}_g \rangle$ for each orientation of the sediment bed, where the angle represents the offset in bed position between the conditioning and erosive flows. Each panel shows $\langle \bar{u}_g \rangle$ at increasing steps-up in flow speed and Shields stress, with τ_* and τ_*/τ_{*cr} reported. Error bars indicate the 95% confidence interval computed over eight trials. The faint horizontal gray dotted line is drawn at the $\langle \bar{u}_g \rangle$ of the unconditioned control case and is intended to assist with visual comparison of the $\langle \bar{u}_g \rangle$ of the different bed orientations to the control.

Once the bed has experienced a subcritical conditioning flow, the mean grain velocity exhibits a dependence on the direction of the subsequent erosive flow. In cases where the conditioning flow and erosive flow occur in the same direction (i.e., 0° offset), we see a reduction in mean grain velocity at Shields stresses up to and including the nominal critical value (Figure 5a, 5b, 5c). This reduction in sediment motion due a history of unidirectional flows agrees with prior studies (e.g., Galanis et al., 2022), although we note that this effect is largely indistinguishable from the unconditioned control case in our experiments once the strength of the erosive flow was increased to stresses above critical (Figure 5d–5i). This pattern is consistent for the case where the erosive flow direction is at an angle of 45° relative to the conditioning flow. The mean grain velocity of the 45° offset is lower than the unconditioned control case, but higher than the unidirectional case (0° offset) for shear stresses up to critical (Figure 5a, 5b). However, the mean grain velocity of the 45° offset is otherwise comparable to the unconditioned control case for the critical and higher Shields stresses (Figure 5c–5i).

The inverse trend occurs for flows that advance from the reversed (180°) or nearly reversed (135°) direction relative to the conditioning flow. In these cases with flow reversals (both 180° and 135°), the mean grain velocity is higher than the unconditioned

control case for all Shields stress increments used in the erosive flow. This behavior is consistent with prior experiments that observed weakening when granular beds are exposed to an above-critical flow from a reversed direction (Galanis et al., 2022; Cúñez et al., 2022). We note that when the erosive flow advances from 135° to the conditioning flow, the bed appears weaker with higher mean grain velocities than the full 180° reversal case for Shields stresses above $\tau_* \geq 0.039$ (Figure 5e–5i).

Lastly, for erosive flow directions that are perpendicular to the conditioning flow (90° offset), we observe mean grain velocities that are generally similar to, or slightly higher than, the unconditioned control case. These higher grain velocities tend to occur once the Shields stress has reached $\tau_* \geq 0.045$ (Figure 5g, 5h, 5i). Additionally, for these higher bed stresses, we note that the 95% confidence interval of the perpendicular case tends to be greater than the control, indicating that the mean grain velocity experiences greater variability at these conditions.

3.3 Higher-Order Statistics of Grain Velocities

Mean grain velocity $\langle \bar{u}_g \rangle$ is a bulk statistic describing the behavior of all identified grains. Thus, it is difficult to determine whether increases in $\langle \bar{u}_g \rangle$ are due to more grains being entrained, these entrained grains having higher velocities, or both. To disentangle these phenomena, we can turn to the full probability density function (PDF) of instantaneous streamwise grain velocities measured for all identified grains in each frame of our videos.

These grain velocity PDFs in Figure 6 show a peak at $u_g = 0$ cm/s with increasingly heavy tails for larger Shields stresses. The cluster of instantaneous velocity measurements around $u_g = 0$ cm/s are due to grains that are mostly immobile but jiggling slightly about their stable locations, especially at or below the onset of motion. This distribution of motions tends to be strongly peaked and symmetric around $u_g = 0$ cm/s, as fluctuations in the flow drive jiggling motions, but not sustained downstream transport. As the fluid stress applied to the sediment bed increases, more and more grains begin to be entrained and transported downstream. The stochastic and independent mobilization of individual grains into active bedload is reflected in the exponential tail of the PDF (Roseberry et al., 2012; Furbish & Schmeeckle, 2013). To account for both grain motions at and just above the onset of motion, we describe the full PDF with a mixture model that incorporates a Student's t-distribution fit to the inner core and an exponential distribution fit to the heavier-than-Gaussian tails (Salevan et al., 2017).

This mixture model is given by

$$P(u_g) = A\frac{\Gamma\left(\frac{\zeta+1}{2}\right)}{\sigma\sqrt{\zeta\pi}\,\Gamma\left(\frac{\zeta}{2}\right)}\left[\frac{\zeta + \left(\frac{u_g}{\sigma}\right)^2}{\zeta}\right]^{\left(-\frac{\zeta+1}{2}\right)} + BH(u_g)\frac{1}{u_g^*}e^{\left(-\frac{u_g}{u_g^*}\right)}, \tag{4}$$

where A is the relative weight of the t-distribution core; B is the relative weight of the exponential tail (where $A+B=1$); σ indicates the characteristic width of the t-distribution and is related to the magnitude of grain velocity fluctuations; ζ is the heaviness of the t-distribution tails; and u_g^* is a characteristic velocity associated with the mobilized grains. We note that when ζ is small, the tails are heavier than a Gaussian with the same variance; when $\zeta \to \infty$, the t-distribution approaches a Gaussian with standard deviation σ. Additionally, Γ is the gamma function and H is the Heaviside function (so that the exponential component of the mixture model is only present for positive grain velocities). We fit this model to our grain velocity PDFs using a standard nonlinear least-squares algorithm.

We focus on the parameters B and u_g^*, which provide information on the grains mobilized as bedload; the parameters σ and ζ are indicative of grain jiggling. B represents the relative quantity of grains mobilized in bedload transport. The data in Figure 7 show

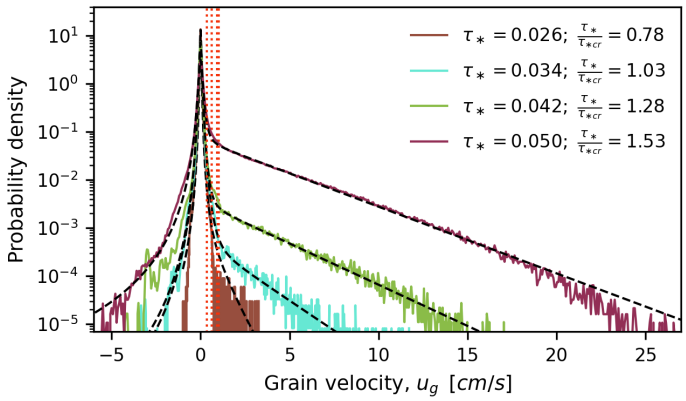

Figure 6. Grain velocity PDFs, $P(u_g)$, measured at four flow velocity intervals for an example unconditioned control case (solid curves). Black dashed curves are fits to the mixture model in Equation 4. The vertical red dotted lines indicate the threshold velocities used to determine whether a grain should be considered active for each velocity interval. This method is discussed further in Section 3.4; for reference, the threshold velocities are $u_g = 0.93$ cm/s, $u_g = 1.0$ cm/s, $u_g = 0.61$ cm/s, and $u_g = 0.34$ cm/s for the increasing Shields stresses listed in the figure legend.

B for each orientation of the sediment bed relative to the flume. We observe that as bed stress increases, the fraction of mobilized grains increases as well; this trend is observed for all orientations (control, 0°, 45°, 90°, 135°, 180°).

The fraction of mobilized grains for each orientation generally displays a similar pattern to the behavior of the mean grain velocity $\langle \bar{u}_g \rangle$ (Figure 5). Compared to the unconditioned control case, we observe a lower B for the 0° and 45° cases below the nominal critical Shields stress (Figure 7a, 7b), a higher B for the 135° and 180° cases at the critical and higher flow velocity intervals (Figure 7c–7i), and a comparable B for the 90° case. Additionally, similar to the behavior of the mean grain velocity $\langle \bar{u}_g \rangle$, we note that when the erosive flow advances from 135° relative to the conditioning flow, the bed appears weaker with higher B than the full 180° reversal case for Shields stresses above $\tau_* \geq 0.039$ (Figure 7e–7i). Lastly, we note that B for the 135° and 180° cases is comparable to or lower than the unconditioned control case for flow velocity intervals below critical (Figure 7a, 7b).

The parameter u_g^* represents the characteristic velocity of the *mobilized* grains. The data in Figure 8 show u_g^* for each orientation of the sediment bed within the flume test section. We observe that as bed stress increases, the characteristic bedload velocity increases as well for all orientations (control, 0°, 45°, 90°, 135°, and 180°). u_g^* generally displays a pattern similar to the behavior of the mean grain velocity, $\langle \bar{u}_g \rangle$ (Figure 5). The unidirectional stress history case (0° offset) exhibits a lower u_g^* than the unconditioned control case for fluid stresses up to $\tau_* < 0.05$ (Figure 8a–8h). The 45° and 90° flow directions have u_g^* comparable to the unconditioned case, while the reversed (180°) and nearly reversed (135°) flow directions are faster than the unconditioned control case for almost all fluid stresses. Interestingly, u_g^* is the parameter that most clearly exhibits a directional dependence on the conditioning flow direction, with strengthening under the unidirectional conditioning flow (0° offset) and a weakening when conditioning and erosive flows are reversed (180° offset) or nearly reversed (135° offset). While we might expect that the characteristic bedload velocity scales with the bulk flow dynamics, which is history independent and the same regardless of bed orientation, we note that this difference in u_g^* for the forward and reverse cases aligns with observations made by Galanis

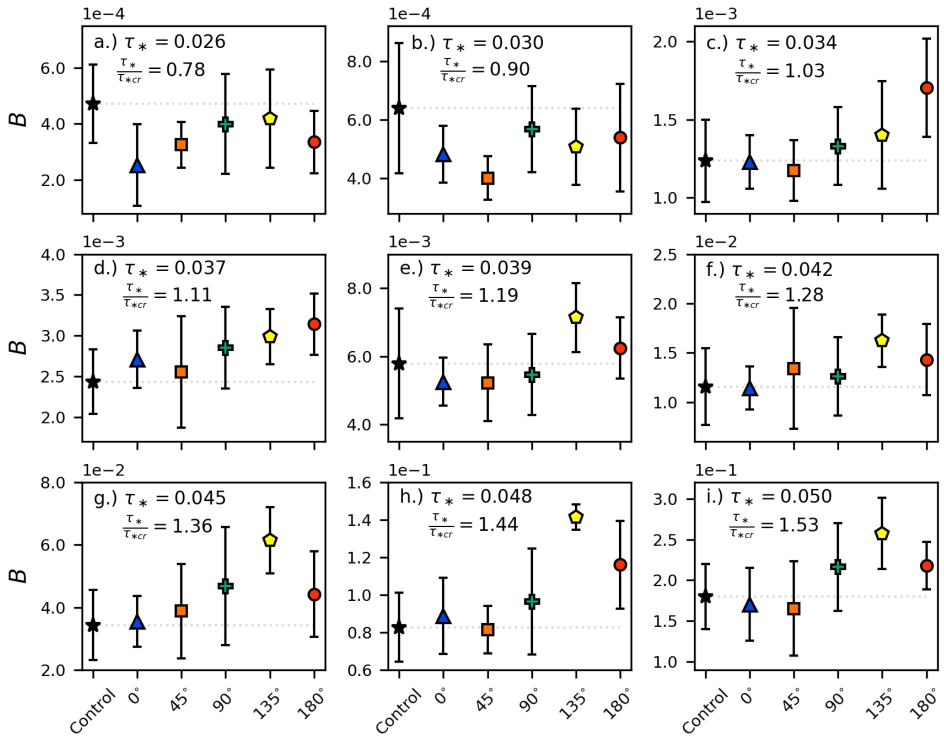

Figure 7. The relative fraction of mobilized grains, B, for each offset angle between the conditioning and erosive flows. Each panel shows B at increasing steps-up in fluid shear and Shields stress, with τ_* and τ_*/τ_{*cr} reported. Error bars indicate the 95% confidence interval calculated over eight trials. The faint horizontal gray dotted line is drawn at B of the unconditioned control case and is intended to assist with visual comparison of B for the different bed orientations to the control.

et al. (2022), who proposed that subtle differences in bed topography may account for these changes.

3.4 Grain Activity

To quantify grain activity, we can simply count the number of active grains in a given frame per unit area as described in section 3.1. However, an "active" grain can be difficult to define. Many studies have taken the approach of first choosing a velocity threshold to identify grains that are in motion (Roseberry et al., 2012; González et al., 2017). The selection of this velocity threshold, however, can appear arbitrary and impacts subsequent analysis (Salevan et al., 2017); further, the magnitude of the selected velocity threshold may neglect states of grain activity like jiggling, where grains move in place without significant forward motion (Rebai et al., 2024). Since we are primarily interested in grains moving as bedload, we defined this threshold velocity for grain activity as the grain velocity where the relative contribution of the Student's t-distribution and exponential distribution are equal. This threshold velocity was calculated by identifying the intersection between the Student's t-distribution with parameters A, ζ, and σ and exponential distribution with parameters B and u_g^*, as determined by fitting to the mixture model in Equation 4. Thus, the threshold velocity for grain activity that we choose represents the transition from predominantly motionless or jiggling grain behavior to predominantly bedload. The threshold velocity for grain activity is shown in Figure 6. We

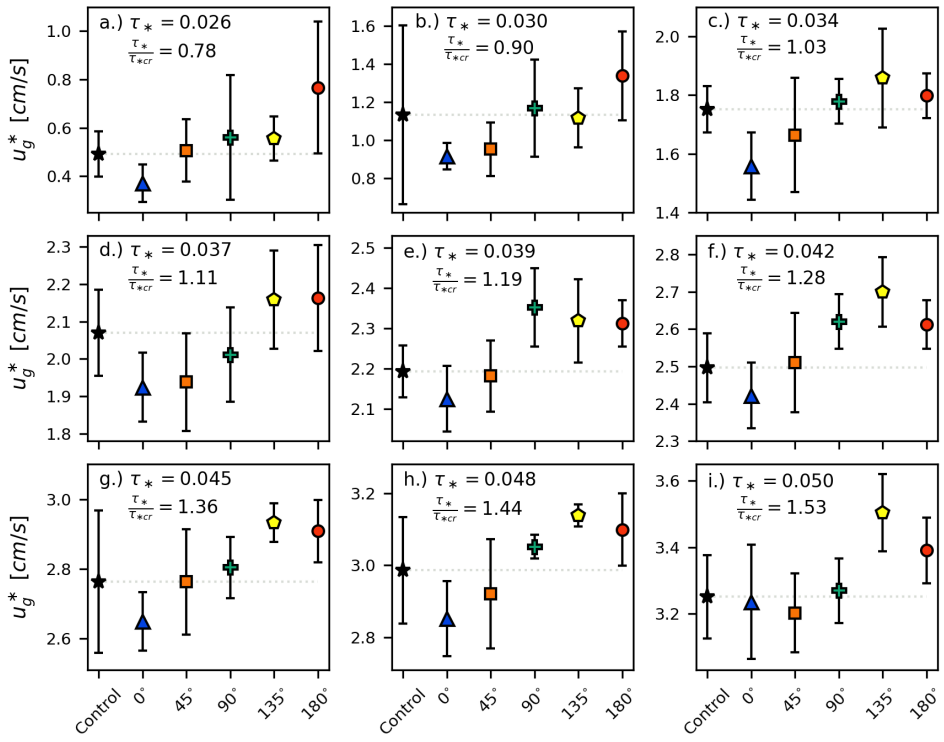

Figure 8. The characteristic bedload velocity, u_g^*, for each offset angle between the conditioning and erosive flows. Each panel shows u_g^* at increasing steps-up in fluid shear and Shields stress, with τ_* and τ_*/τ_{*cr} reported. Error bars indicate the 95% confidence interval calculated over eight trials. The faint horizontal gray dotted line is drawn at u_g^* of the unconditioned control case and is intended to assist with visual comparison of u_g^* for the different bed orientations to the control. We note that values of u_g^* tend to be unreliable below the onset of motion (Salevan et al., 2017).

note that as Shields stress increases and the exponential tails of the grain velocity PDFs become increasingly prominent, the threshold velocity for grain activity decreases.

The data in Figure 9 show the grain activity $\langle \bar{n}_g \rangle$ for each orientation of the sediment bed. For all orientations, grains become more active as bed stress increases. Compared to the unconditioned control case, we observe lower grain activity for the 0° and 45° cases below the nominal critical Shields stress (Figure 9a, 9b). Grain activity is typically higher for the 135° and 180° cases for all Shields stress increments. Grain activity for the 90° case is generally comparable to the unconditioned control. These results for the grain activity reflect observations of B, which represents the relative proportion of grains moving as bedload (Figure 7). Since both B and $\langle \bar{n}_g \rangle$ reflect the quantity of mobile grains, we compared these parameters and observed that they are linearly related (Figure 10).

3.5 Higher-Order Statistics of Grain Activity

While grain activity $\langle \bar{n}_g \rangle$ is a useful metric for describing the quantity of mobile grains per unit area averaged over a video, we can further analyze bed behavior by treating each frame as an instantaneous sample of the number of active grains, N_g. Thus, over an entire video, we can generate a PDF of the number of instantaneously active grains

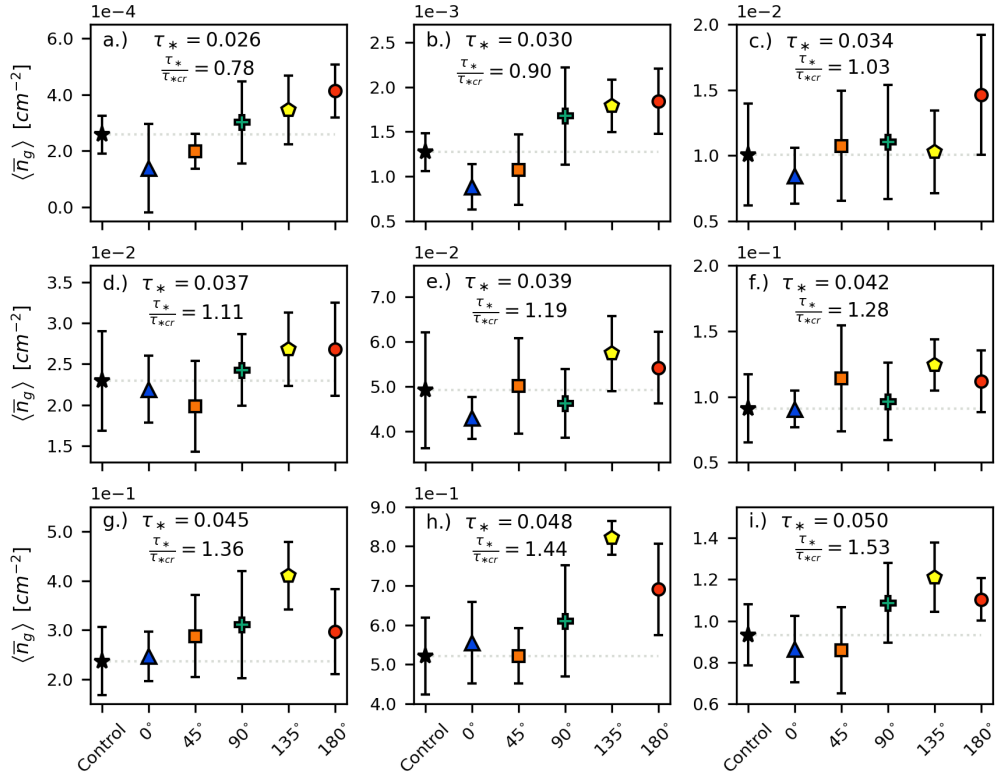

Figure 9. Grain activity of all identified grains $\langle \bar{n}_g \rangle$ for each orientation of the sediment bed, where the angle represents the offset in bed position between the conditioning and erosive flows. Each panel represents $\langle \bar{n}_g \rangle$ at increasing steps-up in flow speed and Shields stress, with τ_* and τ_*/τ_{*cr} reported. Error bars indicate the 95% confidence interval computed over eight trials. The faint horizontal gray dotted line is drawn at $\langle \bar{n}_g \rangle$ of the unconditioned control case and is intended to assist with visual comparison of $\langle \bar{n}_g \rangle$ for the different bed orientations to the control.

(Figure 11). While some studies fit a negative binomial distribution to the PDF of N_g (Ancey et al., 2006), we follow the methodology of González et al. (2017), who fit the Gamma distribution to their PDF of active grains, defined as

$$P(N_g) = \frac{1}{\theta^k \Gamma(k)} N_g^{k-1} e^{-\frac{N_g}{\theta}}, \tag{5}$$

where k is a shape parameter and θ is a scale parameter. The mean number of active grains is thus given by $\langle N_g \rangle = k\theta$ and standard deviation is $std(N_g) = \theta\sqrt{k}$. The reason for selecting the continuous Gamma distribution instead of its discrete counterpart (i.e., the negative binomial distribution) is as follows. When $k < 1$, the Gamma distribution exhibits exponential behavior, which we can see for lower Shields stresses at or below the threshold of motion; in this regime there is a high likelihood that no grains are mobile in any given frame (Figure 11a, 11b). When $k > 1$, the Gamma distribution shifts to behavior that qualitatively appears more log-normal, when a non-zero number of grains are likely to be mobile in a given frame, which occurs at higher Shields stresses (Figure 11c, 11d). This shift in behavior of the Gamma function at $k = 1$ represents a transition in the behavior of the sediment bed from a state where no grains are instantaneously in motion (i.e., $k < 1$) to a regime where at least some grains are in motion at all times (i.e., $k > 1$).

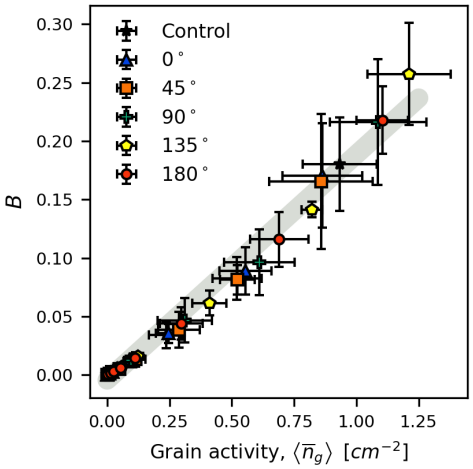

Figure 10. The grain activity for all sediment bed orientations at all Shields stress increments plotted against the B parameter from Equation 4. The error bars represent the 95% confidence interval for both parameters. The gray shaded area indicates a linear best fit between $\langle \bar{n}_g \rangle$ and B given by $B = 0.19\langle \bar{n}_g \rangle - 0.0043$.

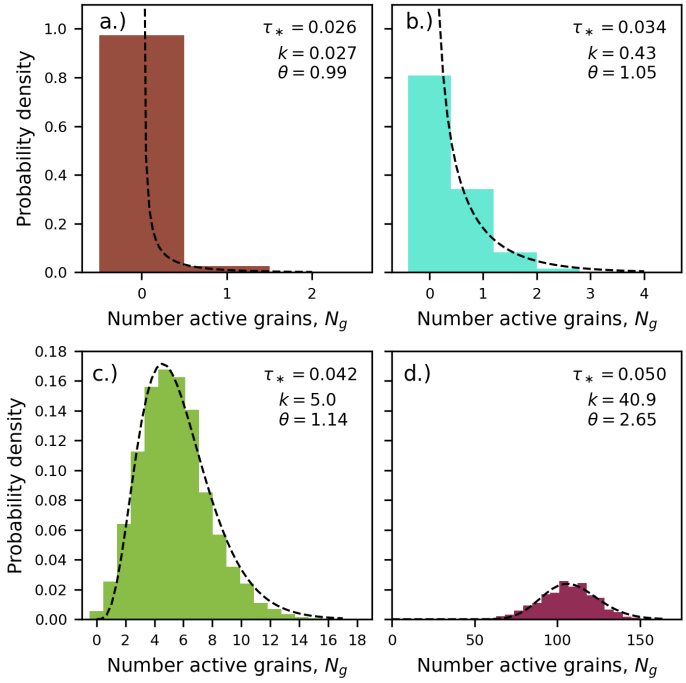

Figure 11. PDF of the number of active grains in each frame of a video of the sediment bed. Dashed lines are best fits of these PDFs to a gamma distribution (Equation 5).

For the various experimental runs, we find the shape parameter k of the best-fit Gamma distribution for the active grains in each video as shear stress is increased from below to above the onset of grain motion. We can then compute a linear best fit and extrapolate the Shields stress where $k = 1$. Although the Shields stress $\tau_{*\,(k=1)}$ of this transition in bed behavior does not necessarily represent the threshold of motion, we find that $\tau_{*\,(k=1)} = 0.037$ is comparable to the nominal critical Shields stress $\tau_{*cr} = 0.033$

for the unconditioned sediment bed. Further, $\tau_{*\,(k=1)}$ gives a single Shields stress value that can readily be compared amongst the experimental cases, while τ_{*cr} can be more challenging to determine (e.g., Salevan et al., 2017). When we compare $\tau_{*\,(k=1)}$ across the five orientations of the sediment bed within the flume, we observe a clear (albeit small) angular dependence (Figure 12). There is a 2.3% increase in $\tau_{*\,(k=1)}$ for the unidirectional case (0° offset) and a 2.4% decrease for the reversed case (180° offset) when compared to the unconditioned control. This observation confirms the trend shown in measurements of mean grain velocity $\langle \bar{u}_g \rangle$ and characteristic bedload velocity u_g^*, with the greatest strengthening occurring when the conditioning and erosive flow are aligned (0° offset) and the greatest weakening when the conditioning and erosive flow are reversed (180° offset). Further, we see that the 90° case, where the erosive flow advances from a perpendicular direction to the conditioning flow, is comparable to the unconditioned control but demonstrates greater variability.

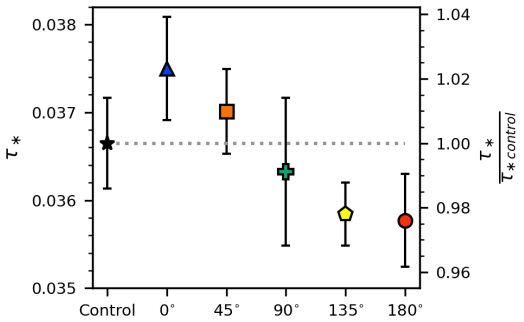

Figure 12. Shields stress $\tau_{*\,(k=1)}$ at the transition in Gamma distribution behavior for bed mobility. Error bars indicate the 95% confidence interval over 8 trials. The right ordinate axis represents $\tau_{*\,(k=1)}$ normalized by $\tau_{*\,(k=1)}$ for the unconditioned control case, with the gray dotted line intended to assist with visual comparison.

4 Discussion

Although the data we collected show that bed erodibility is dependent on directional flow (and therefore stress) history, we note that the signal of bed strengthening under unidirectional flows does not persist at higher flow velocities. In our experiments, this strengthening effect is most pronounced in the 0° case (and the 45° case to a lesser extent) for Shields stresses at and below the nominal critical value. We can confirm that the bed is indeed becoming less mobile by examining the reduction in mean grain velocity $\langle \bar{u}_g \rangle$ and grain activity $\langle \bar{n}_g \rangle$ over the 20 minute conditioning flow (Figure 4). However, as the flow velocity begins to exceed the critical value for sediment motion, the bed behavior approaches that of the unconditioned control case for mean grain velocity $\langle \bar{u}_g \rangle$, B, and grain activity $\langle \bar{n}_g \rangle$.

It is difficult to determine whether our observations of a lack of sustained strengthening above the onset of motion is indeed anomalous, as many previous stress history studies focus either on geophysical contexts by using gravel bed material with a wide grain size distribution (e.g., Masteller & Finnegan, 2017; A.-M. Ockelford & Haynes, 2013; Haynes & Pender, 2007) such that effects such as armoring or size segregration may occur, or on granular physics contexts using nearly monodisperse and smooth glass spheres in small-scale flumes (e.g., Charru et al., 2004; Cúñez et al., 2022). The most analogous study we found in the literature is that of Paphitis and Collins (2005), who used a narrow grain size distribution of natural sand as bed material and an inset sediment bed with dimensions 40 cm by 30 cm by 2.5 cm. Paphitis and Collins (2005) observed an increase in crit-

ical Shields stress ranging from approximately 5–10% in two experimental cases where a 0.387 mm and a 0.774 mm sand bed was subjected to a 20 minute conditioning flow at 77–83% of the critical Shields stress. However, Paphitis and Collins (2005) did not extend their flow velocity significantly above critical; thus, they may have observed a similar saturation of mean grain velocity and activity had they increased their bed stress further above threshold. It seems that few prior stress history studies extended their erosive flows significantly above threshold; however, Galanis et al. (2022), who use monodisperse glass spheres in a small-scale flume, observed a distinct trend of bed strengthening that persisted above the onset of motion.

It is also possible that the selected conditioning flow magnitude and duration were ineffective for producing sustained strengthening. The roles that both magnitude and duration play in the development of stress history effects are not fully understood; indeed, a study by Monteith and Pender (2005) suggested that the relationship between conditioning flow magnitude and bed stability may not be monotonic, with certain conditioning magnitudes being less effective at producing bed strengthening than those either higher or lower. In fact, based on their results, it appears that a conditioning flow at approximately 75-80% of critical is least effective at strengthening the bed for conditioning periods in the range of 20 minutes (although we recognize that their experiments are not a direct comparison to ours as they used a graded gravel bed). Paphitis and Collins (2005), who used a similar bed material and experimental setup as ours, observe greater strengthening at higher conditioning flow magnitudes.

Bed weakening under reversed flows, while less studied, has also previously been observed by Galanis et al. (2022) and Cúñez et al. (2022). The signal of weakening in beds conditioned by a reversed flow (180°) and offset to the reversed flow (135°) is much more evident for flows above critical in our experiments. It is intriguing that the signal of bed weakening is so much more evident than that of bed strengthening, especially given that the same magnitude and duration were used for all conditioning flows. It is possible that this effect is due to the method we used to smooth and prepare the bed. As described above, before each experimental run, we stirred the sand bed and then dragged a mesh screen across the bed surface. The mesh screen was always dragged in the downstream direction; this may also have imparted a stress history that limited bed strengthening and promoted bed erosion when the orientation of the sediment bed was reversed. Interestingly, for nearly all metrics, the 135° case appears weaker than the 180° case, exhibiting the greatest grain mobility and grain velocity. It is unclear why the 135° orientation is consistently more erodible; a possibility is the ability of grains to more easily move around others that have been strengthened by the conditioning flow when the erosive flow is not completely reversed, but more research is required to explain this observation definitively.

Regardless, the directional dependence we observe suggests that the mechanism for storing memory in our granular bed must have an anisotropic component. Previous experiments have typically attributed stress history to smoothing of the bed due to relocation of protruding grains (Masteller & Finnegan, 2017) or compaction (Paphitis & Collins, 2005; Charru et al., 2004); these effects, however, would be isotropic, and so cannot fully explain our results. Cúñez et al. (2022) recently conducted stress history experiments using both reversed and oscillating flows and identified both compaction and shear jamming as mechanisms for memory storage. As our experiments only observe the surface of the sediment bed, we cannot distinguish whether the source of the anisotropy we observed is due to subsurface phenomena such as shear jamming or the formation of force chains through preferential loading of grain contacts, or a surface phenomenon where grains are wedged into pockets that are preferentially supported from only certain directions. We note that these strengthening and weakening effects impact both the quantity of mobilized grains and their characteristic grain velocity, suggesting that this mechanism ex-

tends beyond the surface configuration alone and continues to impact a grain's interaction with the bed even once it is mobilized.

A logical follow-up question to this analysis is whether we can cast the sediment transport rate in terms of the quantities we have measured. In steady-state conditions, the sediment transport rate q_s can be defined as the product of a mean grain velocity and a grain concentration (Lajeunesse et al., 2010; Bridge & Dominic, 1984; Wiberg & Dungan Smith, 1989; Parker et al., 2003; Seminara et al., 2002; Wong et al., 2007). Using terms we have obtained from our experiments, we can take the mean grain velocity to be the characteristic bedload velocity u_g^* determined using the best-fit mixture model to the instantaneous grain velocity measurements (Equation 4). We can determine grain concentration using the grain activity $\langle \bar{n}_g \rangle$ and the volume of a typical grain $\sim D^3$. Using these quantities, the bedload transport rate would then be given by

$$q_s = cD^3 u_g^* \langle \bar{n}_g \rangle. \tag{6}$$

Additionally, since we determine grain activity using a population of fluorescent-painted grains and assume that this population accurately reflects the entirety of the bed, we may need to add a correction factor c accounting for the ratio of painted to unpainted grains at the surface. Lastly, given appropriate calibration, the parameter B obtained from the best-fit mixture model could potentially be used in place of grain activity. Thus, the bedload transport rate could entirely be calculated based on a statistical characterization using the grain velocity PDF.

5 Conclusion

To summarize, we used a rotating sand bed apparatus to develop directional stress history in the sediment bed. We did this by conditioning the sediment bed for 20 minutes at a flow that delivered 80% of the critical shear stress to the bed, then rotating the sediment bed, and finally subjecting it to an erosive flow. We find that the onset of motion is influenced by the angular direction of a conditioning flow relative to the bed-mobilizing flow. Strengthening behavior was observed when the conditioning and erosive flows advance from the same or similar direction (i.e., 0° and 45°); however, this behavior is less evident for bed stresses above the nominal critical value. Weakening behavior was observed when the erosive flow advances from a reversed or nearly reversed direction relative to the conditioning flow (i.e., 180° and 135°). The case where the erosive flow advances from the direction perpendicular to the conditioning flow (i.e., 90°) exhibits similar behavior to the unconditioned control case, but with greater variability.

These results support the existence of an anisotropic component for the mechanism that stores memory in granular beds. Although we cannot determine whether the memory originates from a surface-level or subsurface mechanism, bed strengthening and weakening impacts both the quantity of mobile grains, as well as the velocity of the bedload. Also, since the bedload velocity is greater for weaker beds, sediment flux is likely higher in systems with reversals, even if the threshold of motion may not have changed significantly. This result has implications for predicting bedload transport rates in systems that may be prone to flow reversals, such as tidally-influenced environments, flooding that advances in atypical directions, and rivers with unique hydrologic conditions (Sowby & Siegel, 2025). Additionally, our results suggest new approaches for time-dependent modeling of sediment transport (e.g., Masteller et al., 2024).

Finally, we confirm the usefulness of statistical analyses of bedload behavior. Using both grain velocity and grain activity PDFs, we have shown that we are able to extract useful metrics like a characteristic bedload velocity and thresholds for changes in bed behavior that are possibly representative of the onset of motion. These metrics show clear distinctions between our various experimental cases and may potentially be useful when calculating sediment flux.

Open Research Section

All relevant data and code used to generate the figures in this paper are deposited in figshare, a free and open repository. These datasets can be accessed using the following link: https://figshare.com/s/353da8aef8ecb9a45d98 (Bodek et al., 2025).

Acknowledgments

Financial support was provided by the Army Research Office (ARO Award #W911NF-23-1-0032). The authors thank Bill Sabala for his assistance with the design and fabrication of the rotating sediment dish apparatus, M. Colin Marvin and Mathieu Lapotre for assistance with grain size measurements, Stanford Research Computing for computational support through the Sherlock cluster, and Claire Masteller for helpful discussions.

References

Allen, B., & Kudrolli, A. (2018). Granular bed consolidation, creep, and armoring under subcritical fluid flow. *Physical Review Fluids*, *3*(7), 074305.

Ancey, C., Böhm, T., Jodeau, M., & Frey, P. (2006, July). Statistical description of sediment transport experiments. *Phys. Rev. E*, *74*(1), 011302. doi: 10.1103/PhysRevE.74.011302

Ashida, K., & Michiue, M. (1973). Studies on bed-load transport rate in open channel flows. *IN: SEDIMENT TRANSPORTATION, VOLUME 1*.

Behringer, R. P., & Chakraborty, B. (2018, November). The physics of jamming for granular materials: a review. *Rep. Prog. Phys.*, *82*(1), 012601. doi: 10.1088/1361-6633/aadc3c

Bi, D., Zhang, J., Chakraborty, B., & Behringer, R. P. (2011, December). Jamming by shear. *Nature*, *480*(7377), 355–358. doi: 10.1038/nature10667

Bodek, S., Wang, D., Shattuck, M. D., O'Hern, C. S., & Ouellette, N. T. (2025). Grain velocities from anisotropic stress history experiments. *figshare [dataset]*. doi: https://figshare.com/s/353da8aef8ecb9a45d98

Bridge, J. S., & Dominic, D. F. (1984, April). Bed Load Grain Velocities and Sediment Transport Rates. *Water Resour. Res.*, *20*(4), 476–490. doi: 10.1029/WR020i004p00476

Buffington, J. M., & Montgomery, D. R. (1997, August). A systematic analysis of eight decades of incipient motion studies, with special reference to gravel-bedded rivers. *Water Resour. Res.*, *33*(8), 1993–2029. doi: 10.1029/96WR03190

Cameron, S. M., Nikora, V. I., & Witz, M. J. (2020, April). Entrainment of sediment particles by very large-scale motions. *J. Fluid Mech.*, *888*, A7. doi: 10.1017/jfm.2020.24

Cates, M. E., Wittmer, J. P., Bouchaud, J.-P., & Claudin, P. (1998, August). Jamming, Force Chains, and Fragile Matter. *Phys. Rev. Lett.*, *81*(9), 1841–1844. doi: 10.1103/PhysRevLett.81.1841

Charru, F., Mouilleron, H., & Eiff, O. (2004, November). Erosion and deposition of particles on a bed sheared by a viscous flow. *J. Fluid Mech.*, *519*, 55–80. doi: 10.1017/S0022112004001028

Clark, A. H., Shattuck, M. D., Ouellette, N. T., & O'Hern, C. S. (2017, March). Role of grain dynamics in determining the onset of sediment transport. *Phys. Rev. Fluids*, *2*(3), 034305. doi: 10.1103/PhysRevFluids.2.034305

Cúñez, F. D., Franklin, E. M., Houssais, M., Arratia, P., & Jerolmack, D. J. (2022, June). Strain hardening by sediment transport. *Phys. Rev. Res.*, *4*(2), L022055. doi: 10.1103/PhysRevResearch.4.L022055

Dey, S. (1999, May). Sediment threshold. *Appl. Math. Model.*, *23*(5), 399–417. doi: 10.1016/S0307-904X(98)10081-1

Diplas, P., Dancey, C. L., Celik, A. O., Valyrakis, M., Greer, K., & Akar, T. (2008, October). The Role of Impulse on the Initiation of Particle Movement Under Turbulent Flow Conditions. *Science*, *322*(5902), 717–720. doi: 10.1126/science.1158954

Einstein, H. A., & El-Samni, E.-S. A. (1949, July). Hydrodynamic Forces on a Rough Wall. *Rev. Mod. Phys.*, *21*(3), 520–524. doi: 10.1103/RevModPhys.21.520

Engelund, F., & Fredsøe, J. (1976). A sediment transport model for straight alluvial channels. *Hydrology Research*, *7*(5), 293–306.

Escauriaza, C., González, C., Williams, M. E., & Brevis, W. (2023, March). Models of bed-load transport across scales: turbulence signature from grain motion to sediment flux. *Stochastic Environ. Res. Risk Assess.*, *37*(3), 1039–1052. doi: 10.1007/s00477-022-02333-9

Ferdowsi, B., Ortiz, C. P., Houssais, M., & Jerolmack, D. J. (2017, November). River-bed armouring as a granular segregation phenomenon. *Nat. Commun.*, *8*(1363), 1–10. doi: 10.1038/s41467-017-01681-3

Furbish, D. J., & Schmeeckle, M. W. (2013, March). A probabilistic derivation of the exponential-like distribution of bed load particle velocities. *Water Resour. Res.*, *49*(3), 1537–1551. doi: 10.1002/wrcr.20074

Galanis, M., Shattuck, M. D., O'Hern, C. S., & Ouellette, N. T. (2022, January). Directional strengthening and weakening in hydrodynamically sheared granular beds. *Phys. Rev. Fluids*, *7*(1), 013802. doi: 10.1103/PhysRevFluids.7.013802

García, M. H. (2013, May). Sediment Transport and Morphodynamics. *Sedimentation Engineering*, 21–163. doi: 10.1061/9780784408148.ch02

Gomez, B. (1983, October). Temporal Variations in the Particle Size Distribution of Surficial Bed Material: The Effect of Progressive Bed Armouring. *Geogr. Ann. Ser. A Phys. Geogr.*, *65*(3-4), 183–192. doi: 10.1080/04353676.1983.11880085

González, C., Richter, D. H., Bolster, D., Bateman, S., Calantoni, J., & Escauriaza, C. (2017, February). Characterization of bedload intermittency near the threshold of motion using a Lagrangian sediment transport model. *Environ. Fluid Mech.*, *17*(1), 111–137. doi: 10.1007/s10652-016-9476-x

Haynes, H., & Pender, G. (2007, April). Stress History Effects on Graded Bed Stability. *J. Hydraul. Eng.*, *133*(4), 343–349. doi: 10.1061/(ASCE)0733-9429(2007)133:4(343)

Houssais, M., Ortiz, C. P., Durian, D. J., & Jerolmack, D. J. (2015). Onset of sediment transport is a continuous transition driven by fluid shear and granular creep. *Nature communications*, *6*(1), 6527.

Kelley, M., Mahon, R. C., Ganti, V., Daas, D., & Leary, K. (2023). *Linking particle trajectories to changes in bedform 3-dimensionality.* AGU Fall Meeting. (Poster EP41D-2341)

Kirchner, J. W., Dietrich, W. E., Iseya, F., & Ikeda, H. (1990, August). The variability of critical shear stress, friction angle, and grain protrusion in water-worked sediments. *Sedimentology*, *37*(4), 647–672. doi: 10.1111/j.1365-3091.1990.tb00627.x

Lajeunesse, E., Malverti, L., & Charru, F. (2010, December). Bed load transport in turbulent flow at the grain scale: Experiments and modeling. *J. Geophys. Res. Earth Surf.*, *115*(F4). doi: 10.1029/2009JF001628

Lavelle, J. W., & Mofjeld, H. O. (1987). Do critical stresses for incipient motion and erosion really exist? *Journal of Hydraulic Engineering*, *113*(3), 370–385.

Luque, R. F., & Van Beek, R. (1976, April). Erosion And Transport Of Bed-Load Sediment. *Journal of Hydraulic Research*. Retrieved from `https://www.tandfonline.com/doi/abs/10.1080/00221687609499677`

Majmudar, T. S., & Behringer, R. P. (2005, June). Contact force measurements and stress-induced anisotropy in granular materials. *Nature*, *435*(7045), 1079–1082. doi: 10.1038/nature03805

Mao, L. (2018, December). The effects of flood history on sediment transport in gravel-bed rivers. *Geomorphology*, *322*, 196–205. doi: 10.1016/j.geomorph.2018.08.046

Mao, L., Dell'Agnese, A., Huincache, C., Penna, D., Engel, M., Niedrist, G., & Comiti, F. (2014, June). Bedload hysteresis in a glacier-fed mountain river. *Earth Surf. Processes Landforms*, *39*(7), 964–976. doi: 10.1002/esp.3563

Masteller, C. C., & Finnegan, N. J. (2017, January). Interplay between grain protrusion and sediment entrainment in an experimental flume. *J. Geophys. Res. Earth Surf.*, *122*(1), 274–289. doi: 10.1002/2016JF003943

Masteller, C. C., Finnegan, N. J., Turowski, J. M., Yager, E. M., & Rickenmann, D. (2019, March). History-Dependent Threshold for Motion Revealed by Continuous Bedload Transport Measurements in a Steep Mountain Stream. *Geophys. Res. Lett.*, *46*(5), 2583–2591. doi: 10.1029/2018GL081325

Masteller, C. C., Johnson, J. P. L., Rickenmann, D., & Turowski, J. M. (2024, December). Modeling memory in gravel-bed rivers: A flow history-dependent relation for evolving thresholds of motion. *EGUsphere*, 1–18. doi: 10.5194/egusphere-2024-3250

Meyer-Peter, E., & Müller, R. (1948). Formulas for bed-load transport. In *Iahsr 2nd meeting, stockholm, appendix 2.*

Monteith, H., & Pender, G. (2005, December). Flume investigations into the influence of shear stress history on a graded sediment bed. *Water Resour. Res.*, *41*(12). doi: 10.1029/2005WR004297

Mordant, N., Crawford, A. M., & Bodenschatz, E. (2004, June). Experimental Lagrangian acceleration probability density function measurement. *Physica D*, *193*(1), 245–251. doi: 10.1016/j.physd.2004.01.041

Ockelford, A., Woodcock, S., & Haynes, H. (2019, November). The impact of inter-flood duration on non-cohesive sediment bed stability. *Earth Surf. Processes Landforms*, *44*(14), 2861–2871. doi: 10.1002/esp.4713

Ockelford, A.-M., & Haynes, H. (2013, June). The impact of stress history on bed structure. *Earth Surf. Processes Landforms*, *38*(7), 717–727. doi: 10.1002/esp.3348

Oldmeadow, D. F., & Church, M. (2006). A field experiment on streambed stabilization by gravel structures. *Geomorphology*, *78*(3-4), 335–350.

O'Riordan, C. A., Monismith, S. G., & Koseff, J. R. (1993, December). A study of concentration boundary-layer formation over a bed of model bivalves. *Limnol. Oceanogr.*, *38*(8), 1712–1729. doi: 10.4319/lo.1993.38.8.1712

Ouellette, N. T., Xu, H., & Bodenschatz, E. (2006, February). A quantitative study of three-dimensional Lagrangian particle tracking algorithms. *Exp. Fluids*, *40*(2), 301–313. doi: 10.1007/s00348-005-0068-7

Pähtz, T., Clark, A. H., Valyrakis, M., & Durán, O. (2020, March). The Physics of Sediment Transport Initiation, Cessation, and Entrainment Across Aeolian and Fluvial Environments. *Rev. Geophys.*, *58*(1), e2019RG000679. doi: 10.1029/2019RG000679

Papanicolaou, A. N., Diplas, P., Dancey, C. L., & Balakrishnan, M. (2001, March). Surface Roughness Effects in Near-Bed Turbulence: Implications to Sediment Entrainment. *J. Eng. Mech.*, *127*(3), 211–218. doi: 10.1061/(ASCE)0733-9399(2001)127:3(211)

Paphitis, D., & Collins, M. B. (2005, August). Sand grain threshold, in relation to bed 'stress history': an experimental study. *Sedimentology*, *52*(4), 827–838. doi: 10.1111/j.1365-3091.2005.00710.x

Parker, G. (1979, September). Hydraulic Geometry of Active Gravel Rivers. *Journal of the Hydraulics Division*, *105*(9), 1185–1201. doi: 10.1061/JYCEAJ.0005275

Parker, G., & Klingeman, P. C. (1982, October). On why gravel bed streams are paved. *Water Resour. Res.*, *18*(5), 1409–1423. doi: 10.1029/

WR018i005p01409

Parker, G., Seminara, G., & Solari, L. (2003, July). Bed load at low Shields stress on arbitrarily sloping beds: Alternative entrainment formulation. *Water Resour. Res.*, *39*(7). doi: 10.1029/2001WR001253

Phillips, C. B., & Jerolmack, D. J. (2016, May). Self-organization of river channels as a critical filter on climate signals. *Science*, *352*(6286), 694–697. doi: 10.1126/science.aad3348

Pretzlav, K. L. G., Johnson, J. P. L., & Bradley, D. N. (2020, November). Smartrock Transport in a Mountain Stream: Bedload Hysteresis and Changing Thresholds of Motion. *Water Resour. Res.*, *56*(11), e2020WR028150. doi: 10.1029/2020WR028150

Radice, A., Sarkar, S., & Ballio, F. (2017, July). Image-based Lagrangian Particle Tracking in Bed-load Experiments. *Journal of Visualized Experiments : JoVE*(125), 55874. doi: 10.3791/55874

Rebai, D., Radice, A., & Ballio, F. (2024, August). Traveling or Jiggling: Particle Motion Modes and Their Relative Contribution to Bed-Load Variables. *J. Geophys. Res. Earth Surf.*, *129*(8), e2024JF007637. doi: 10.1029/2024JF007637

Recking, A., Liébault, F., Peteuil, C., & Jolimet, T. (2012, June). Testing bedload transport equations with consideration of time scales. *Earth Surf. Processes Landforms*, *37*(7), 774–789. doi: 10.1002/esp.3213

Reid, I., Frostick, L. E., & Layman, J. T. (1985, January). The incidence and nature of bedload transport during flood flows in coarse-grained alluvial channels. *Earth Surf. Processes Landforms*, *10*(1), 33–44. doi: 10.1002/esp.3290100107

Roseberry, J. C., Schmeeckle, M. W., & Furbish, D. J. (2012, September). A probabilistic description of the bed load sediment flux: 2. Particle activity and motions. *J. Geophys. Res. Earth Surf.*, *117*(F3). doi: 10.1029/2012JF002353

Roth, D. L., Finnegan, N. J., Brodsky, E. E., Cook, K. L., Stark, C. P., & Wang, H. W. (2014, October). Migration of a coarse fluvial sediment pulse detected by hysteresis in bedload generated seismic waves. *Earth Planet. Sci. Lett.*, *404*, 144–153. doi: 10.1016/j.epsl.2014.07.019

Salevan, J. C., Clark, A. H., Shattuck, M. D., O'Hern, C. S., & Ouellette, N. T. (2017, November). Determining the onset of hydrodynamic erosion in turbulent flow. *Phys. Rev. Fluids*, *2*(11), 114302. doi: 10.1103/PhysRevFluids.2.114302

Seminara, G., Solari, L., & Parker, G. (2002, November). Bed load at low Shields stress on arbitrarily sloping beds: Failure of the Bagnold hypothesis. *Water Resour. Res.*, *38*(11), 31-1–31-16. doi: 10.1029/2001WR000681

Shields, A. (1936). Application of similarity principles and turbulence research to bed-load movement.

Shim, J., & Duan, J. G. (2017, March). Experimental study of bed-load transport using particle motion tracking. *Int. J. Sediment Res.*, *32*(1), 73–81. doi: 10.1016/j.ijsrc.2016.10.002

Slotterback, S., Mailman, M., Ronaszegi, K., van Hecke, M., Girvan, M., & Losert, W. (2012, February). Onset of irreversibility in cyclic shear of granular packings. *Phys. Rev. E*, *85*(2), 021309. doi: 10.1103/PhysRevE.85.021309

Sowby, R. B., & Siegel, A. C. (2025, February). Unusual Drainages of the Americas. *Water Resour. Res.*, *61*(2), e2024WR039824. doi: 10.1029/2024WR039824

Sumer, B. M., Chua, L. H. C., Cheng, N.-S., & Fredsøe, J. (2003, August). Influence of Turbulence on Bed Load Sediment Transport. *J. Hydraul. Eng.*, *129*(8), 585–596. doi: 10.1061/(ASCE)0733-9429(2003)129:8(585)

Turowski, J. M., Badoux, A., & Rickenmann, D. (2011, February). Start and end of bedload transport in gravel-bed streams. *Geophys. Res. Lett.*, *38*(4). doi: 10.1029/2010GL046558

Wiberg, P. L., & Dungan Smith, J. (1989, January). Model for Calculating Bed

Load Transport of Sediment. *J. Hydraul. Eng.*, *115*(1), 101–123. doi: 10.1061/(ASCE)0733-9429(1989)115:1(101)

Wiberg, P. L., & Smith, J. D. (1987). Calculations of the critical shear stress for motion of uniform and heterogeneous sediments. *Water resources research*, *23*(8), 1471–1480.

Wong, M., & Parker, G. (2006). Reanalysis and correction of bed-load relation of meyer-peter and müller using their own database. *Journal of Hydraulic Engineering*, *132*(11), 1159–1168.

Wong, M., Parker, G., DeVries, P., Brown, T. M., & Burges, S. J. (2007, March). Experiments on dispersion of tracer stones under lower-regime plane-bed equilibrium bed load transport. *Water Resour. Res.*, *43*(3). doi: 10.1029/2006WR005172

Yager, E. M., Venditti, J. G., Smith, H. J., & Schmeeckle, M. W. (2018). The trouble with shear stress. *Geomorphology*, *323*, 41–50.